


Coupling Microkinetics with Continuum Transport Models to Understand Electrochemical CO₂ Reduction in Flow Reactors

Nitish Govindarajan^{1,†}, Tiras Y. Lin^{2,†}, Thomas Roy^{2,†}, Christopher Hahn,¹ and Joel B. Varley^{1,*}

¹Materials Science Division, Lawrence Livermore National Laboratory, Livermore, California 94550, USA

²Computational Engineering Division, Lawrence Livermore National Laboratory, Livermore, California 94550, USA

 (Received 19 May 2023; revised 3 July 2023; accepted 24 July 2023; published 21 August 2023)

We present a multiscale approach that couples *ab initio* microkinetic simulations and two-dimensional (2D) continuum transport models to study electrochemical CO₂ reduction to CO on Au electrodes in a flow reactor configuration. We find the key parameters, including CO₂ concentration, *pH*, the current density towards CO, and the Tafel slopes, to strongly depend on the applied potential and position on the electrode. We find a rapid decrease in the CO₂ concentration and current density towards CO as a function of electrode position. We further discuss two strategies to improve CO₂ availability: increasing the shear or flow rate of CO₂ and the introduction of a defect in between the electrode. In both cases, increased CO₂ availability results in increased CO current density at the higher potentials. We find good agreement between a 1D continuum transport model with an effective boundary layer thickness corresponding to the shear rate used for the 2D simulations. Finally, we provide a phenomenological model that can be used instead of the microkinetic model to accelerate the multiscale simulations when extended to higher dimensions and more complicated reactor geometries.

DOI: [10.1103/PRXEnergy.2.033010](https://doi.org/10.1103/PRXEnergy.2.033010)

I. INTRODUCTION

Electrochemical CO₂ reduction (eCO₂R) is a promising approach for the sustainable production of fuels and chemicals using renewable electricity [1]. With the development of CO₂ electrolysis gaining momentum in the past decade, significant progress has been made in understanding how factors such as the electrode composition, electrolyte *pH*, CO₂ availability, temperature, mass transport, and electrolyte composition affect the reaction rate and efficiency [2]. Despite these promising advances, we are still faced with several challenges that have to be overcome in order to enable the commercialization and cost-effective operation of CO₂ electrolyzers [3]. For instance, the electrochemical conversion of CO₂ towards high-value C₂₊ products like ethylene, ethanol, and propanol still suffers from low-energy efficiencies (i.e., high overpotentials) and product selectivity on state-of-the-art Cu-based catalysts

[4]. Simpler eCO₂R products like CO can be produced at industrially relevant current densities (> 300 mA/cm²) with high selectivity on Au and Ag-based catalysts. However, mass transport limitations due to low CO₂ availability and loss of CO₂ as carbonate, the competing hydrogen evolution reaction, and factors affecting long-term stability (surface reconstruction and/or poisoning, salt deposition, and bubble formation) at typical operating conditions still remain major challenges [5–7]. A lot of these challenges are a result of the existing gaps in resolving the reaction environment at the vicinity of the electrode, which was shown to be crucial in obtaining accurate mechanistic insights [8] and in controlling the overall performance of eCO₂R [9,10].

In parallel with the experimental progress, modeling studies from the atomistic to the continuum levels have also greatly improved the overall understanding of eCO₂R. For instance, atomistic simulations based on density functional theory (DFT) and microkinetic modeling have provided crucial insights into the complex reaction pathways and mechanisms involved in eCO₂R [11], identifying the rate- and selectivity-determining steps towards the various eCO₂R products [12–15], and understanding mechanisms behind electrolyte effects (e.g., electrolyte *pH*, cations, and anions) on eCO₂R [16,17]. Similarly, continuum models have also provided important insights into the structure of

*varley2@llnl.gov

†These authors contributed equally to this work.

Published by the American Physical Society under the terms of the [Creative Commons Attribution 4.0 International](https://creativecommons.org/licenses/by/4.0/) license. Further distribution of this work must maintain attribution to the author(s) and the published article's title, journal citation, and DOI.

the electrical double layer, transport phenomena, and the spatial and temporal distribution of key parameters that control reactor performance [18–21]. Although microkinetic simulations provide detailed information on coverages of reaction intermediates, intrinsic activity of sites, and reaction pathways, they typically do not account for (i) diffusion of CO₂ across the boundary layer, (ii) the buffer equilibria involving CO₂, (iii) the changes in the pH at the vicinity of the electrode during eCO₂R, and (iv) double layer charging effects, all of which have been shown to drastically affect CO₂ availability and influence reactivity near the electrode surface [8,20]. These observations therefore necessitate the coupling of activities and coverages of species predicted using *ab initio*-based microkinetic simulations with concentrations of species involved in the reaction from continuum transport models that account for (i)–(iv) to be able to fully resolve the reaction environment at the vicinity of the electrode surface and obtain unbiased insights into eCO₂R. Such a coupling was successfully performed with a one-dimensional (1D) transport model to study eCO₂R on Au by Ringe *et al.* [8], and on Ag by Singh *et al.* [22].

In this work, we present a multiscale modeling approach that couples *ab initio* microkinetic simulations with two-dimensional (2D) continuum transport models that account for electrolyte flow, migration, diffusion, buffer equilibria, and finite ion size effects to study electrochemical CO₂ reduction to CO on Au electrodes. We find the key parameters of eCO₂R including the CO₂ concentration and pH at the electrode, the current density towards CO (j_{CO}), and the simulated Tafel slopes to strongly depend on both the applied potential and the position along the electrode. We further discuss two strategies to improve CO₂ utilization: increasing the shear/flow rate of CO₂ and the introduction of a defect in the middle of the electrode. In both cases, we observe an increase in j_{CO} due to increased CO₂ availability in the mass-transport-limited regimes. We obtain good agreement between the results of the 2D simulations and a 1D model. Finally, we develop a phenomenological Butler-Volmer-like model to estimate j_{CO} that can be used instead of the microkinetic simulations in future studies involving more complex geometries. Our work presents an important step toward the development of multidimensional, multiscale modeling approaches needed to capture the full complexity of electrochemical processes including eCO₂R and beyond.

II. RESULTS AND DISCUSSION

A. Description of the model system and coupling framework

Figure 1(a) shows a schematic of the reactor configuration with a volumetric flow rate Q between the planar cathode and the anode, representing an aqueous flow reactor. In this study, we focus on the eCO₂R reaction at the

cathode (Au) of length L ($L = 1$ cm), as shown in Fig. 1(b), and we note that the configuration considered is different from more complex configurations such as the gas diffusion electrode, which would have a qualitatively different fluid flow. The velocity profile within the full reactor is parabolic, i.e., plane Poiseuille flow, as shown in Fig. 1(a). However, since we are primarily interested in mass transfer near the cathode surface, and the mass transfer boundary layer is expected to be thin, i.e., the Schmidt number here is large, we approximate the velocity profile as a linear shear flow with shear rate $\dot{\gamma}$. This mass transfer problem was previously considered in Ref. [23] for simplified reaction kinetics. We consider $\dot{\gamma}$ ranging from 0.1 to 100 ($\times 1.91$ s⁻¹), which corresponds to Péclet numbers

$$\text{Pe} = \dot{\gamma}L^2/D_{\text{CO}_2} \quad (1)$$

ranging from 10⁴–10⁷, where D_{CO_2} is the diffusivity of CO₂. The Péclet number here provides a measure of the relative importance of flow to diffusion. To provide some intuition on these shear rates, we estimate that, for a channel of 1-cm width and 1-cm height, the corresponding flow rates Q are approximately 1.91–1910 mL/min. Note that while we consider this full range of Péclet numbers in our analysis, the highest Péclet number likely corresponds to a physically unattainable flow rate. We also estimate the expected boundary layer thickness (d_{BL}) averaged over the cathode according to [23]

$$d_{\text{BL}}/L \approx a \text{Pe}^{-1/3}, \quad (2)$$

where $a = 3^{2/3}\Gamma(1/3)/4$.

The continuum transport equations are solved on a 2D mesh, with the coupling between microkinetics and continuum transport (see the Appendix for details) performed at each point on the reactive (cathode) boundary, i.e., $y = 0$, in a self-consistent manner [see Fig. 1(c) and the Appendix section for details on the coupling scheme]. The key parameters exchanged during the coupling scheme at the boundary ($[\text{CO}_2]_{y=0}$, $p\text{H}_{y=0}$, potential $\phi_{y=0}$, and j_{CO}) are also highlighted. In what follows, we present results obtained from the coupled 2D simulations of eCO₂R to CO on Au electrodes.

B. Variation in the key parameters with applied potential and electrode position

Figure 2 shows the variations in the key reaction parameters with the applied potential (U) from the coupled microkinetic simulations and the 2D continuum transport model. The results correspond to flow with $\text{Pe} = 10^5$ ($Q = 19.1$ mL/min). The solid lines and the shaded regions indicate the average value and variation of the parameter along the length of the electrode, respectively. As can be seen in Fig. 2(a), the CO₂ concentration at the electrode

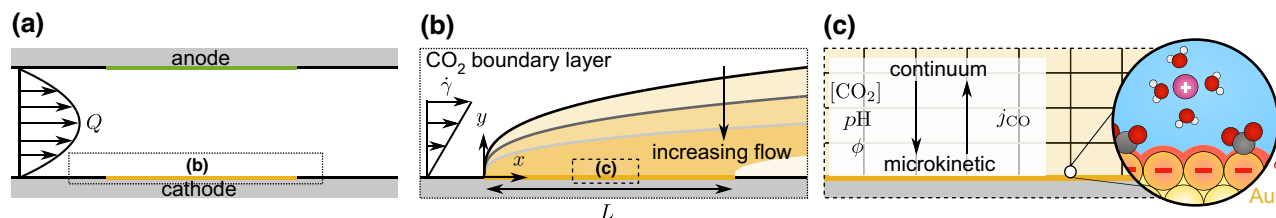


FIG. 1. (a) Schematic of the reactor configuration considered, where a volumetric flow rate Q flows between two plates. In this study, we focus on the mass transfer phenomena near the cathode of length L ($L = 1$ cm), as highlighted in (b). Near the cathode, the velocity profile can be approximated as a shear flow with shear rate $\dot{\gamma}$. A boundary layer of depleted CO_2 concentration is shown schematically. (c) The continuum transport equations are solved on a mesh, where at each point on the reactive (cathode) boundary, coupling with the microkinetic model is performed.

($[\text{CO}_2]_{y=0}$) is much lower than the bulk $[\text{CO}_2]$ even at the lower potentials where the reaction rate of eCO_2R (and therefore the consumption of CO_2) is extremely low. This is due to the inclusion of finite-size effects in the continuum model via the generalized modified Poisson-Nernst-Planck (GMPNP) formalism [see Eqs. (A8), (A9), and (A11)] [24], where the cation (K^+) occupies most of the available volume near the negatively charged electrode. With increasing U , the reaction rate towards eCO_2R increases with concomitant consumption of CO_2 , resulting in a rapid depletion of $[\text{CO}_2]_{y=0}$. Figure 2(b) shows the increase in the $p\text{H}$ at the electrode with U as a result of increased production of OH^- ions during eCO_2R [Eq. (A3)]. Note that the $p\text{H}$ at the electrode is generally lower than the bulk $p\text{H}$ (7.5 for a 0.5-molar KHCO_3 solution) as a result of electrostatic repulsion of anions (OH^-) (and attraction of cations) from the negatively charged electrode. We only observe a higher $p\text{H}$ at the electrode compared to the bulk $p\text{H}$ at potentials < -1.0 V. This observation further points to the importance of the exact definition of “local” in the context of $p\text{H}$, as was also highlighted in a previous study by Bohra *et al.* [20].

The CO partial current density (j_{CO}) obtained from the coupled 2D simulations is shown in Fig. 2(c). There is a variation in the slope of j_{CO} as a result of the change in the rate-determining step (RDS) with U [8], as expected for multistep electrochemical reactions [13] and confirmed by a degree of rate control [25] analysis. (cf. Fig. S2 within the Supplemental Material [26]). A change in the RDS with U also results in changes in the continuous Tafel slopes ($\partial U / \partial \log_{10} j_{\text{CO}}$), as shown in Fig. 2(d). The dashed lines indicate the Tafel slopes obtained from the microkinetic model for the respective RDS in the absence of mass transport effects (i.e., based only on intrinsic kinetics). At potentials higher (less reducing) than about -0.7 V, the $^*\text{COOH} \rightarrow ^*\text{CO}$ step [Eq. (A1c)] limits the overall rate, resulting in an intrinsic Tafel slope of ca. 40 mV/dec. For $U < -0.8$ V, the adsorption of $^*\text{CO}_2$ [Eq. (A1a)] is the RDS, resulting in an increase in the intrinsic Tafel slope as it is the first step in the reaction mechanism (approximately 80–100 mV/dec). The reason for a potential-dependent

Tafel slope in the latter step is the quadratic surface-charge dependence of $^*\text{CO}_2$ adsorption [8]. While the deviations from the intrinsic Tafel slopes are minor at the lower potentials with the $^*\text{COOH} \rightarrow ^*\text{CO}$ step being the RDS, significant deviations are observed at $U \leq -0.8$ V, where the adsorption of CO_2 is the RDS due to the convolution of CO_2 mass transport with the intrinsic kinetics. This deviation is in agreement with the rapid depletion of $[\text{CO}_2]_{y=0}$ with U observed in Fig. 2(a), resulting in mass transport limitations at higher potentials. Here it is worth noting that most experiments for eCO_2R on Au are performed in the potential regions where there is a convolution of intrinsic kinetics with mass transport limitations [27], which could result in incorrect mechanistic interpretations regarding the (potential-dependent) identity of the rate-determining steps. This aspect was particularly highlighted in a recent study by Gregoire *et al.* [28], where hydrodynamics of the reactor strongly affects the measured Tafel slopes for eCO_2R .

We further analyze variations in $[\text{CO}_2]$, j_{CO} , and $p\text{H}$ at the electrode as a function of the position (x) along the electrode for two different potentials ($U = -0.8$ and -1.1 V) for $\text{Pe} = 10^5$, as shown in Figs. 3(a)–3(c). Contour plots showing a more resolved dependence of these parameters on both the applied potential and spatial position along the electrode are included in the Supplemental Material [26] for the studied flow rates. At $U = -0.8$ V, $[\text{CO}_2]$, $p\text{H}$ at the electrode, and j_{CO} remain fairly constant with electrode position. However, for $U = -1.1$ V, we note a rapid decrease in $[\text{CO}_2]$ and j_{CO} with electrode position. This can also be seen in Figs. 3(d)–3(f), with the electrode position on a log scale. An initial reduction is observed within the first nanometer of the electrode, with a further reduction from about 10^{-2} cm until the end of the electrode. The rapid depletion of $[\text{CO}_2]$ with electrode position at $U = -1.1$ V also results in a concomitant increase in the simulated Tafel slopes with electrode position (see Fig. S3 within the Supplemental Material [26]). These observations indicate that having electrodes with smaller lengths might be beneficial, particularly for reactor configurations where flow is stagnant (e.g., H-cells)

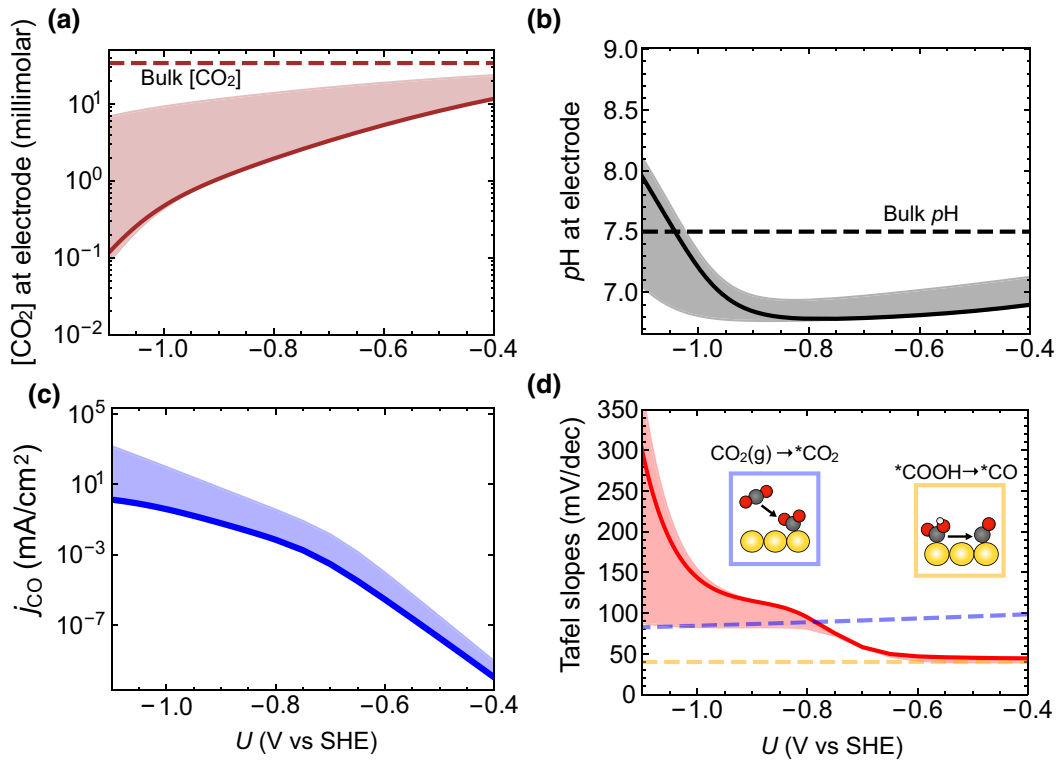


FIG. 2. Variations of the key parameters with the applied potential measured vs the standard hydrogen electrode [U (vs SHE)] for $\text{Pe} = 10^5$ ($\dot{\gamma} = 1.91 \text{ s}^{-1}$, flow rate = 19.1 mL/min). Average values are in solid lines and shaded regions indicate variation along the electrode length. (a) Concentration of CO_2 ($[\text{CO}_2]$) at the interface. Dashed line indicates bulk $[\text{CO}_2]$ (34 millimolar). (b) pH at the interface. Dashed line indicates the bulk pH (7.5). (c) CO current density j_{CO} and (d) the continuous Tafel slopes. Dashed lines indicate the Tafel slopes corresponding to the RDS being $\text{*COOH} \rightarrow \text{*CO}$ (40 mV/dec) and $\text{CO}_2(\text{g}) \rightarrow \text{*CO}_2$ (80–100 mV/dec) from microkinetic simulations in the absence of transport effects.

where there is likely a significant depletion in $[\text{CO}_2]$ with increasing cathodic potentials.

C. Strategies to increase CO_2 availability

We explore two possible strategies to increase CO_2 availability at higher potentials: (i) using the same reactor configuration shown in Fig. 1(b) and changing $\dot{\gamma}$, i.e., the flow rate Q , to the values shown in Table I, and (ii) the introduction of an inert defect at the middle of the electrode.

TABLE I. Summary of the shear rates ($\dot{\gamma}$) used in this study, as well as their corresponding Péclet numbers (Pe), the effective boundary layer thickness (d_{BL}), and the approximate flow rate, assuming a 1-cm-wide channel of 1-cm height.

Shear rate $\dot{\gamma}$ (s^{-1})	Peclet number Pe	Boundary layer d_{BL} (μm)	Flow rate ($1 \times 1 \text{ cm}^2$) Q (mL/min)
0.191	10^4	647	1.91
1.91	10^5	300	19.1
19.1	10^6	139	191
191	10^7	64.7	1910

1. The effect of flow

First, we consider the effect of flow on the CO current density j_{CO} . In Fig. 4, we show the increase or decrease in j_{CO} as a function of Pe relative to the case where $\text{Pe} = 10^5$. As expected, we observe that j_{CO} increases with increasing Pe , and that the effect is magnified as we approach more negative U , i.e., less reaction-limited conditions. When U is small, the effect of flow is expected to be diminished, since $[\text{CO}_2]$ is not sufficiently depleted on the electrode for an increase in flow to be beneficial. We note that the choice of Pe to compare to here is somewhat arbitrary, and that the potential where mass transfer limitations begin to occur is dependent on Pe . Specifically, as Pe increases, a larger potential is required to deplete the $[\text{CO}_2]$ at the electrode, and as a result, the comparisons here are not at equivalent levels of mass transfer resistance. Nevertheless, the comparison in Fig. 4 demonstrates the effect of flow rates.

It is interesting to note that the relative increases in j_{CO} observed in mass-transfer-limited conditions are of a similar order of magnitude to the classical Graetz-Leveque problem, i.e., shear flow of a single species over a perfectly reactive surface [29,30]. In particular, the total reaction is expected to scale as approximately $\text{Pe}^{1/3}$ [23]; as an

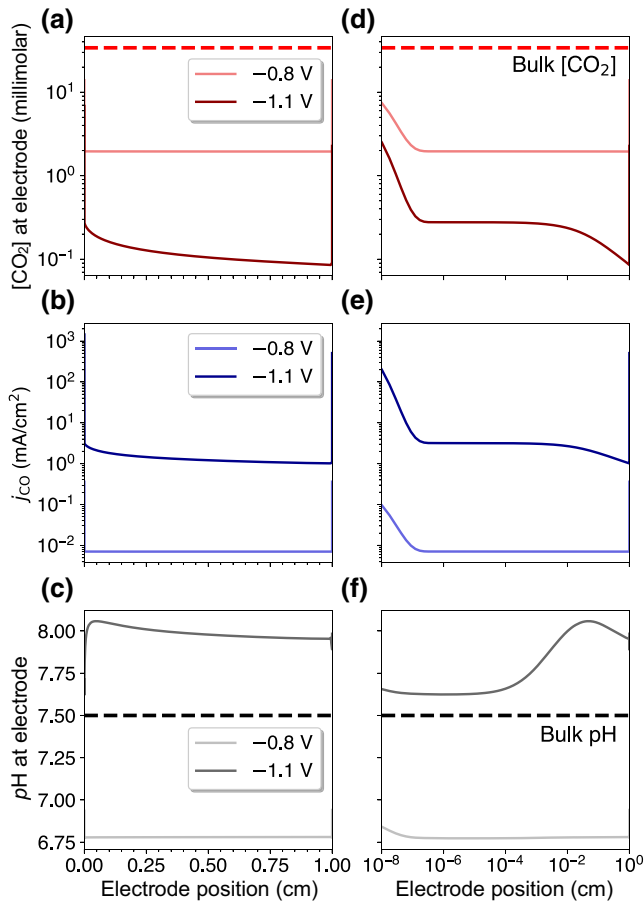


FIG. 3. Variations of the (a) CO_2 concentration at the electrode, (b) CO current density, and (c) pH at the electrode as a function of position (x) along the electrode at $U = -0.8$ and -1.1 V vs SHE for $\text{Pe} = 10^5$. The same variations are shown in (d)–(f), showing the electrode position on a logarithmic scale for better resolution.

example, when Pe is increased from 10^5 to 10^6 , this simple theory would predict the current density to increase by a factor of approximately 2.2. Of course, the problem considered is not expected to match this simple theory exactly, since we have also considered additional physics, such as electromigration and finite-size effects. Nevertheless, it is reassuring that the right order of magnitude is captured.

While we have primarily focused our attention here on the current density j_{CO} , it may be important in many applications to consider the CO_2 single-pass conversion, or in other words, the fraction of CO_2 that is consumed. In certain situations, it may be desirable to have a single-pass conversion near 1. This can be defined as

$$\lambda = \frac{j_{\text{CO}}A/2F}{QC_{\text{CO}_2}^{\text{bulk}}}, \quad (3)$$

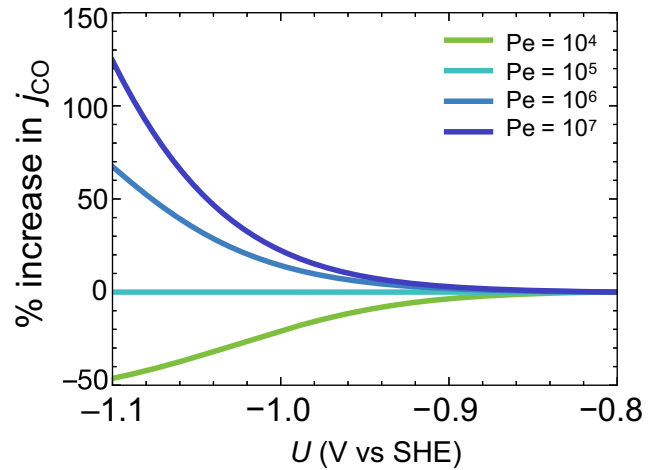


FIG. 4. Effects of different flow rates on j_{CO} , with the increase or decrease shown for the different Pe relative to $\text{Pe} = 10^5$.

where A is the area of the electrode, F is Faraday's constant, and $C_{\text{CO}_2}^{\text{bulk}}$ is the bulk CO_2 concentration. While we have observed j_{CO} to increase with Pe , it certainly increases slower than linearly at large U —the simple theory predicts $\text{Pe}^{1/3}$. Since the flow rate Q scales $\propto \text{Pe}$, the single-pass conversion is expected to approach 0 as the flow rate increases. For the simple theory, we would have $\lambda \sim \text{Pe}^{-2/3}$. Thus, simply trying to achieve ever higher flow rates can have diminishing returns when considering other factors in the overall design and optimization of electrochemical reactors.

2. The effect of an inert defect

We explore a second strategy to increase CO_2 availability, and thus current density j_{CO} : the introduction of an inert defect at the center of the electrode. As shown in Fig. 5(a), we introduce a defect of length $L_{\text{defect}} = 0.1$ cm in between the electrode, resulting in two electrodes of length $L/2$ (i.e., 0.5 cm each). We note that the inert defect being considered is effectively a gap in the electrode without fundamental material properties (e.g. the potential of zero charge, PZC), but this analysis could be extended to consider material properties, including surface charging and electrocatalytic activity that might exhibit stronger influence on the overall performance of the electrode. In Fig. 5(b), we compare $[\text{CO}_2]$ at the electrode at $U = -1.1$ V both when the defect is and is not present; the data for the case of no defect are plotted with an imaginary gap in the middle to facilitate comparison. We observe that there is increased $[\text{CO}_2]$ available to the beginning of the second electrode after the defect. The resulting relative increase in j_{CO} is shown in Fig. 5(c).

The primary mechanism behind the increased $[\text{CO}_2]$ can be explained as follows. As CO_2 flows past the first electrode, the $[\text{CO}_2]$ boundary layer grows in thickness as it is

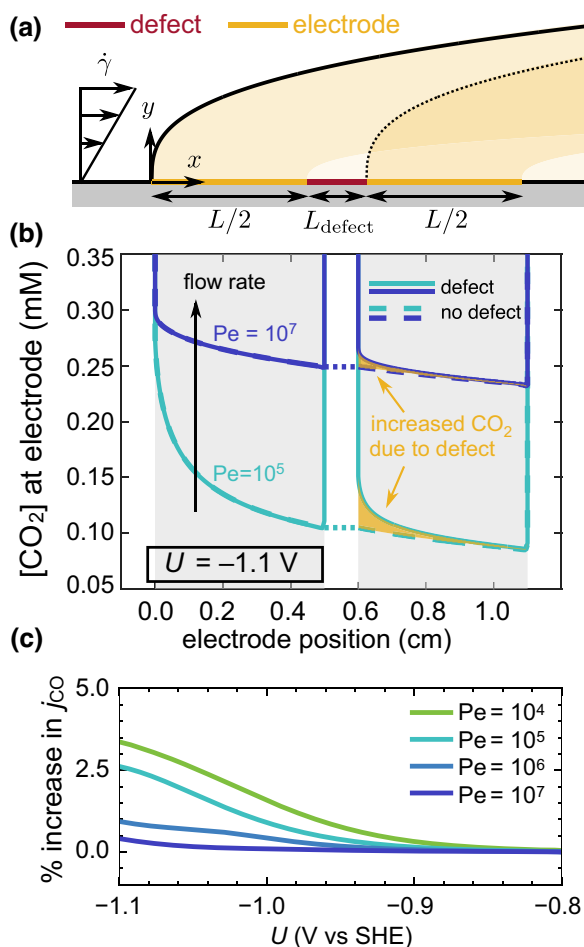


FIG. 5. (a) Schematic of the cathode with an inert defect ($L_{\text{defect}} = 0.1$ cm) in between the two electrodes, each of length 0.5 cm along with the boundary layer of depleted CO_2 . (b) Increase in the $[\text{CO}_2]$ at the interface at $U = -1.1$ V with and without the defect, and with increasing Pe (from 10^5 to 10^7). (c) Percentage increase in j_{CO} with the defect as compared to without, shown for different respective Pe .

continuously used up at the electrode. However, over the inert defect, where no reaction occurs, $[\text{CO}_2]$ is allowed to replenish via diffusion through the boundary layer. At the second electrode, a second boundary layer grows, and $[\text{CO}_2]$ continues to deplete. This interaction between the two $[\text{CO}_2]$ depletion wakes is complex (see, e.g., Refs. [31–33]), and as a result, does not permit a simple theoretical approximation. Like the previous case of no defect, we continue to observe an increase in CO_2 availability at the electrode with increasing flow even in the presence of an inert defect, but the rich relationship between defect, flow, and microkinetics merits further exploration.

While the resulting increase in j_{CO} due to the defect as shown in Fig. 5(c) is relatively modest, it is important to note that increasing j_{CO} in this way also directly results in spatial modifications of the local $p\text{H}$ and a corresponding increase in the single-pass conversion λ . In contrast to the

previous section where we increased the flow rate Q , the denominator of λ does not increase with the addition of the defect [cf. Eq. (3)]. Increasing the flow rate and altering the distribution or patterning of electrode materials, i.e., the addition of defects, are two independent effects that should be balanced depending on whether the ultimate goal is to increase j_{CO} or λ . Additionally, the influence on spatial $p\text{H}$ profiles may be a strategy for tailoring local conditions along the electrode for specific reaction pathways or products, particularly for more complex electrochemical reactions that strongly depend on $p\text{H}$ (e.g., CO_2/CO reduction on Cu) [12–15]. This warrants a need for codesign that simultaneously considers the flow rate and electrode patterning to achieve target outputs in electrochemical flow reactors. It is important to note that, for this study, we have chosen the location and size of the defect arbitrarily, since our goal in this work was to demonstrate how our multiscale framework can handle complex configurations. Future investigations will involve a full study of how the configuration of defects interacts with the flow and the microkinetic model.

D. Comparison with lower-dimensional surrogate models

The state-of-the-art multiscale models that attempt to resolve mass-transport effects typically adopt 1D descriptions that use an analytical Butler-Volmer expression for the boundary condition [19,34], or combine *ab initio*-based microkinetic simulations with continuum mass-transport models [8,35,36]. While these approaches are more computationally tractable, they fail to capture the spatial inhomogeneities in the key reaction parameters observed in this study. This limitation can thereby limit the reliability of such models when attempting to optimize electrode geometries for targeted performance. Nonetheless, lower-dimensional models that can predict product current density and selectivity as a function of operational conditions are still desirable, particularly for other computationally intensive modeling efforts such as topology optimization, where complex flow paths, mass transfer resistances, and intricate electrode geometries can arise that cannot be predicted *a priori* [18,37–39]. Thus, extracting and validating simpler models from two- (or higher-)dimensional models with results obtained in lower dimensions is useful for gauging the regimes at which surrogate models can sufficiently describe the properties of interest.

1. One- versus two-dimensional simulations

We compare the results of our 2D simulations with flow explicitly considered to 1D simulations that assume an effective boundary layer thickness that corresponds to the respective Pe for the 2D simulations (cf. Table I and the Supplemental Material Appendix [26]). As shown in Fig. 6, we find good agreement between the average j_{CO}

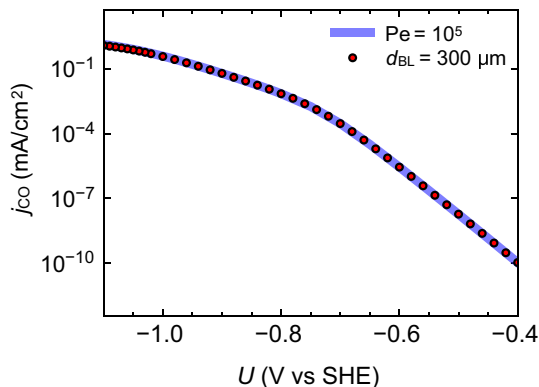


FIG. 6. Comparison between the spatially averaged j_{CO} obtained from the 2D simulation with $\text{Pe} = 10^5$ and a 1D simulation with an effective boundary layer thickness of $300 \mu\text{m}$.

obtained from the 2D simulation and the 1D simulation when the average boundary layer thickness over the electrode is approximated by Eq. (2), where d_{BL} scales as $\text{Pe}^{-1/3}$ [23]. For example, when $\text{Pe} = 10^5$, $d_{\text{BL}} \approx 300 \mu\text{m}$. While this approximation for the boundary layer thickness was derived assuming single species mass transfer, the agreement observed here demonstrates that, even when electromigration, finite-size effects, and more complex kinetics are considered, a 1D simulation can potentially capture the average properties predicted in a 2D simulation as long as the boundary layer thickness is judiciously chosen. Of course, 2D simulations are still required in order to capture the spatial variation of the parameters, which are found to vary strongly over short distance scales (Fig. 3). Furthermore, such a comparison is only straightforward in simple flow configurations like the one considered in this work, and more complex flows, electrode geometries, and electrochemical reaction pathways would merit further investigation.

2. Phenomenological Butler-Volmer model to estimate j_{CO}

While the coupling between the microkinetic simulations and the 2D continuum transport model is efficient for the simple reactor geometries considered in this work, it might be computationally expensive to perform the multi-scale simulations for more complex geometries and/or in three dimensions. Additionally, for computational topology optimization to target specific electrode and reactor designs, the high dimensionality of the parameter space makes the coupling scheme of microkinetic and continuum transport models computationally prohibitive. Crucial for gradient-based optimization algorithms, derivatives are easily obtained for simple expressions such as Eq. (4), but not for an external microkinetic simulation package. This motivates the development of surrogate models that

can replace the microkinetic simulations to help accelerate the coupling scheme. To do so, we fit the j_{CO} and U data obtained from parametric sweeps of $[\text{CO}_2]$ and $p\text{H}$ in microkinetic simulations (without the coupling to continuum transport) to a phenomenological Butler-Volmer-type model. The model has the form [40]

$$\frac{1}{j_{\text{CO}}(U)} = \frac{1}{j_{0,1}e^{\alpha_1 U}} + \frac{1}{j_{0,2}e^{\alpha_2 U}} + \frac{1}{j_{\text{lim}}}, \quad (4)$$

where $j_{0,1}$ and α_1 are the exchange current density and charge-transfer coefficient associated with the first RDS ($^*\text{COOH} \rightarrow ^*\text{CO}$), $j_{0,2}$ and α_2 are the exchange current density and charge-transfer coefficient associated with the second RDS (the adsorption of $^*\text{CO}_2$), and j_{lim} is the limiting current density. We note that $j_{0,1}$, $j_{0,2}$, and j_{lim} depend on $[\text{CO}_2]$ and $p\text{H}$ (see Sec. S2 of the Supplemental Material [26] for further details on the microkinetic sweeps and the fitting procedure). Furthermore, such a simplified model might not be applicable to more complex reactions involving (potential-dependent) adsorbate coverages [41]. We further use the following simplifications while performing the microkinetic sweeps and the coupled 1D simulation: (i) a constant capacitance ($17 \mu\text{F}/\text{cm}^2$) was used in the simulations and (ii) the Frumkin correction that relates to an additional potential drop within the electrochemical double layer obtained from the coupled simulations [8] was neglected. We stress that these simplifications strongly influence the agreement between the coupled 1D simulations and the phenomenological model, and further motivate the need for validating surrogate model results with resolved higher-dimensional models.

Figure 7 shows the contribution of the different terms in Eq. (4) towards j_{CO} evaluated with the $[\text{CO}_2]$ and $p\text{H}$ obtained from the 1D simulation with an effective boundary layer thickness of $300 \mu\text{m}$. At each potential, the largest term in Eq. (4) dominates the overall contribution towards j_{CO} . While the first term dominates for $U \gtrsim -0.55 \text{ V}$ where the $^*\text{COOH} \rightarrow ^*\text{CO}$ is the RDS, the second term dominates at more reducing potentials when the adsorption of $^*\text{CO}_2$ is the RDS. For the 1D models used to compare with Eq. (4), we find that, even though the Tafel slope appears to rapidly increase at the most reducing potentials in Fig. 7, it is clear that the j_{CO} remains far below the fundamental limiting current j_{lim} .

Overall, the j_{CO} predicted from the phenomenological model is in good qualitative agreement with the coupled microkinetics and 1D continuum transport simulation, with the degree of quantitative agreement subject to the assumptions or simplifications mentioned previously. Therefore, such a model could be used instead of the microkinetic model while extending the coupling scheme to more complex geometries and higher dimensions, provided that it has been validated by more resolved and higher-dimensional models, as we have shown here.

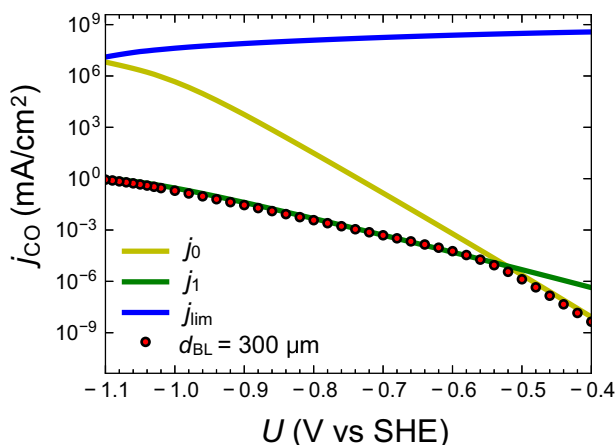


FIG. 7. Contribution of individual terms in the phenomenological Butler-Volmer model towards j_{CO} , plotted with the results from the 1D simulation with an effective boundary layer thickness of 300 μm . Here j_0 and j_1 refer to the currents associated with the first and second terms in Eq. (4), respectively.

III. CONCLUSIONS

By using a multiscale modeling approach that couples *ab initio*-based microkinetic simulations to continuum transport models, we provide a detailed understanding of how the local environment can influence electrochemical reduction reactions in a flow reactor, focusing on CO_2 reduction to CO on Au electrodes. Our approach is able to spatially resolve key reaction parameters, including the CO current density, CO_2 concentration, and $p\text{H}$ at the electrode. We further explore and quantify how these key reaction parameters can be impacted by experimental variables such as flow rate and applied potential, confirming that, while higher flow rates do improve the achievable current densities at a given potential, mass transport effects can limit the utilization of the full electrode length for CO production. Our results show that disruptions of the planar electrode with inert sections or gaps can improve the available CO_2 concentration along the electrode length and offer modest gains in the CO current density that depend on flow rate and potential. This suggests that simple spatial patterning of planar electrodes may be an effective (co)design strategy for improving single-pass conversion efficiencies and help mitigate other constraints set by flow rates and operating conditions. While we focus on CO_2 reduction on Au electrodes in this work, these results are general to a variety of different electrochemical reactions and illustrate the severity of mass-transport limitations encountered in flow reactors. The framework presented in this study of coupling continuum transport with microkinetics is an important step towards future investigations of more complex cell configurations, such as gas diffusion electrodes, where flow patterns may not be as simple. Additionally, we show that this approach can allow for the creation

of informed (condition-aware) surrogate models of lower dimensionality and computational cost that can accelerate the design and optimization of electrochemical flow reactors.

The raw data to reproduce the figures in the article and the open-source software package to perform the coupled microkinetic and transport simulations are available from Zenodo [53,54].

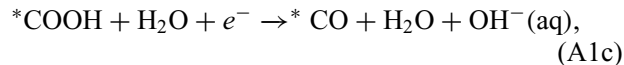
ACKNOWLEDGMENTS

This work was performed under the auspices of the U.S. Department of Energy by Lawrence Livermore National Laboratory (LLNL) under Contract No. DE-AC52-07NA27344, and was partially supported by a Cooperative Research and Development Agreement (CRADA) between LLNL and TotalEnergies American Services, Inc. (affiliate of TotalEnergies SE) under Agreement No. TC02307 and Laboratory Directed Research and Development (LDRD) funding under project 22-SI-006. We acknowledge computational support from the LLNL Institutional Computing Grand Challenge program.

APPENDIX: METHODS

1. Microkinetic simulations

The microkinetic simulations are performed using the steady-state approximation with the open-source and freely available `CaTMAP` software package [42]. The reaction mechanism for eCO_2R considered in the microkinetic simulations is



where the asterisk refers to the active site: the steps on $\text{Au}(211)$. H_2O is the dominant proton donor given the negligible concentration of H_3O^+ under neutral $p\text{H}$ conditions. We do not consider the competing hydrogen evolution reaction (HER) in this study as Au exhibits low partial current densities and Faradaic efficiency (ca. 10%) towards HER in the potential range considered in this work (-0.6 to -1.1 V vs SHE) [8,9]. The surface-charge-density- (σ) dependent energies for the reaction intermediates $*\text{CO}_2$, $*\text{COOH}$, and $*\text{CO}$ in Eq. (A1) used as input to the microkinetic model are taken from Ref. [8]. We refer the reader to

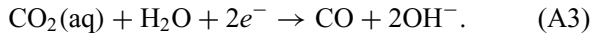
Ref. [8] for further details on the DFT calculations and the microkinetic model. Steps (A1a) and (A1b) are assumed to be well described by the reaction thermodynamics, while step (A1c) includes a (potential-dependent) kinetic barrier with a charge-transfer coefficient of 0.5. In order to convert the per-site turnover frequency (TOF) calculated using CatMAP to a flux, we use the equation

$$\mathbf{J}_i \cdot \mathbf{n} = \rho \text{ TOF}_i, \quad (\text{A2})$$

where \mathbf{J}_i is the flux for species i , \mathbf{n} is the outward normal vector, and ρ is the active site density (9.6×10^{-5} sites/ \AA^2) considering a grain boundary density of $2.873 \mu\text{m}^{-1}$ for polycrystalline Au [8,43].

2. Continuum transport models

One charge-transfer reaction occurs at the cathode surface, eCO_2R , which is assumed to only be CO evolution:



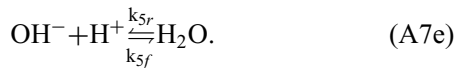
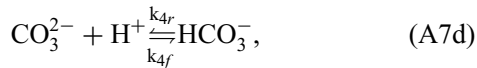
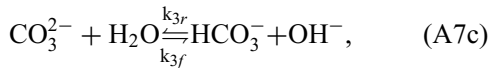
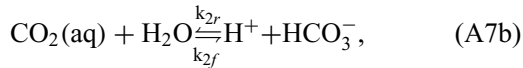
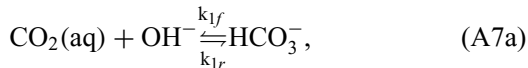
At the cathode surface, the fluxes of the solution species are given by

$$\mathbf{J}_{\text{CO}_2} \cdot \mathbf{n} = \frac{j_{\text{CO}}}{2F}, \quad (\text{A4})$$

$$\mathbf{J}_{\text{OH}^-} \cdot \mathbf{n} = -\frac{j_{\text{CO}}}{F}, \quad (\text{A5})$$

$$\mathbf{J}_i \cdot \mathbf{n} = 0 \quad \text{for } i = \text{HCO}_3^-, \text{CO}_3^{2-}, \text{K}^+, \quad (\text{A6})$$

where \mathbf{n} is again the outward normal vector, F is Faraday's constant, and j_{CO} is the CO current density obtained from Eq. (A2), i.e., $j_{\text{CO}} = F\mathbf{J}_{\text{CO}} \cdot \mathbf{n}$. Note that, for the 2D case, the value of j_{CO} is spatially varying along the length of the cathode surface. The following homogeneous reactions occur in the electrolyte (0.5-molar KHCO_3):



The conservation of mass is given by

$$0 = -\nabla \cdot \mathbf{J}_i + \sum_j R_{j,i}, \quad (\text{A8})$$

where j is the index of the homogeneous reaction given by Eq. (A7), and $R_{j,i}$ is the production rate of species i in the homogeneous reaction j . The flux \mathbf{J}_i of species i is given by the Nernst-Planck equation in a generalized modified form (termed GMPNP) to account for finite-size effects of the electrolyte species:

$$\begin{aligned} \mathbf{J}_i = & -D_i \nabla C_i + C_i \mathbf{u} - \frac{D_i C_i z_i F}{RT} \nabla \phi \\ & - D_i C_i \left(\frac{N_A \sum_i a_i^3 \nabla C_i}{1 - N_A \sum_i a_i^3 C_i} \right), \end{aligned} \quad (\text{A9})$$

where C_i is the concentration of species i , D_i is the diffusion coefficient of species i , \mathbf{u} is the fluid velocity, z_i is the charge of species i , R is the gas constant, T is temperature, ϕ is the ionic potential, N_A is the Avogadro constant, and a_i is the effective solvated diameter of species i (we set $a_i = 0$ for all species except the cation K^+). In the 1D case we have $\mathbf{u} = 0$, and at the bulk we have a Dirichlet condition $C_i = C_i^{\text{bulk}}$ for all species i . In the 2D case, $\mathbf{u} = \gamma \mathbf{y}$, i.e., a shear flow with shear rate γ , as illustrated in Fig. 1(b). At the boundaries for the 2D case, the flux of species i is given by

$$\mathbf{J}_i \cdot \mathbf{n} = \begin{cases} C_i^{\text{bulk}} \mathbf{u} & \text{at the inlet,} \\ C_i \mathbf{u} & \text{at the outlet,} \end{cases} \quad (\text{A10})$$

and $\mathbf{J}_i \cdot \mathbf{n} = 0$ otherwise, except at the cathode surface where it is given by Eqs. (A4)–(A6).

The Poisson equation is

$$-\nabla \cdot (\epsilon_0 \epsilon_r \nabla \phi) = F \sum_i z_i C_i, \quad (\text{A11})$$

where ϵ_0 is the permittivity of vacuum, and $\epsilon_r = 78.4$ is the relative permittivity of water. A Dirichlet condition sets the potential $\phi = 0$ at the bulk, and, for the 2D case, a Neumann condition sets the flux $\nabla \phi \cdot \mathbf{n} = 0$ at the inlet, outlet, and inactive surface. As done in Refs. [8,44], we use the following Robin boundary condition for the potential at the electrode surface:

$$\epsilon_0 \epsilon_r \nabla \phi \cdot \mathbf{n} = C_{\text{gap}} (U - U^{\text{PZC}} - \phi). \quad (\text{A12})$$

Here C_{gap} is the gap capacitance (we consider $C_{\text{gap}} = 20 \mu\text{F}/\text{cm}^2$), U is the cell potential, and U^{PZC} is the PZC of the working electrode relative to the reference electrode (we consider $U^{\text{PZC}} = 0.16 \text{ V}$ vs SHE) [8]. Together, Eqs. (A8), (A9), and (A11) are called the GMPNP equations [24]. The PNP equations can be recovered by taking $a_i = 0$.

The continuum model is implemented using the open-source finite element library `firedrake` [45] in the `EchemFEM` package [46,47]. Standard piecewise-linear

```

1  $\Delta j_{\text{CO}} \leftarrow \infty$ ;
2  $j_{\text{CO}}, j_{\text{CO}}^{(0)} \leftarrow 0$ ;
3  $\mathbf{Y} \leftarrow C_i = C_i^{\text{bulk}}, \phi = 0$ ;
4  $\mathbf{Y}, \mathbf{Y}^{(0)}, \mathbf{Y}^{(1)} \leftarrow \text{continuum}(j_{\text{CO}}, \mathbf{Y})$ ;
5 while  $\Delta j_{\text{CO}} > \text{tol}$  do
6    $\mathbf{Y} \leftarrow (1 - \theta_0 - \theta_1)\mathbf{Y} + \theta_0\mathbf{Y}^{(0)} + \theta_1\mathbf{Y}^{(1)}$ ;
7   for node k on cathode boundary do
8      $(j_{\text{CO}})_k \leftarrow \text{mkm}(\mathbf{Y})_k$ ;
9   end
10   $\mathbf{Y}^{(1)} \leftarrow \mathbf{Y}^{(0)}$ ;
11   $\mathbf{Y}^{(0)} \leftarrow \mathbf{Y}$ ;
12   $\mathbf{Y} \leftarrow \text{continuum}(j_{\text{CO}}, \mathbf{Y})$ ;
13   $\Delta j_{\text{CO}} \leftarrow \frac{\|j_{\text{CO}} - j_{\text{CO}}^{(0)}\|_{L^2}}{\|j_{\text{CO}}\|_{L^2}}$ ;
14   $j_{\text{CO}}^{(0)} \leftarrow j_{\text{CO}}$ ;
15 end

```

Algorithm 1. Iterative coupling sketch

elements are used for spatial discretization (on quadrilateral cells for the 2D simulations). Typically used to tackle the advective term in the advection diffusion equation, streamline upwind Petrov-Galerkin stabilization [48,49] is used here on the combined advection migration flux (see the Supplemental Material [26] for discretization details).

3. Coupling between continuum and microkinetic modeling

To complete the continuum model defined in Appendix A2, the boundary conditions (A4) and (A5) require j_{CO} values at each boundary point. In one dimension, this is a single value, but in two dimensions, it is for every mesh node on the cathode boundary (for a piecewise-linear flux along the cathode). Values for j_{CO} are obtained from solving the microkinetic model described in Appendix A1. For closure, this model requires surface values for CO_2 concentration, pH, and potential ϕ , which are all obtained from the solution of the continuum model.

We solve the coupled continuum-microkinetic model in an iterative manner as outlined in Algorithm 1. In the algorithm, j_{CO} refers to the piecewise-linear current density of CO along the cathode surface, and \mathbf{Y} refers to the solution vector of the continuum model, i.e., concentrations C_i of all species i and the potential ϕ . The operation $\text{continuum}(j_{\text{CO}}, \mathbf{Y})$ refers to numerically solving the continuum model with CO current density j_{CO} , and using \mathbf{Y} as the initial guess for the Newton solver. The operation $\text{mkm}(\mathbf{Y})_k$ refers to solving the microkinetic model with input values C_{CO_2} , pH, and ϕ from the solution vector \mathbf{Y} at node k . The relaxation parameters θ_0, θ_1 , where $\theta_0 + \theta_1 < 1$, help with the stability of the iterative scheme.

Because of the nonlinearity of the continuum model, Newton's method will not converge at higher cathodic potential when starting from a constant initial guess. Instead, we use a continuation strategy where cathodic

potential is increased incrementally, such that the initiation of CO current density and the solution vector \mathbf{Y} is done using the values of the previous voltage (replacing lines 2 and 3).

-
- [1] P. D. Luna, C. Hahn, D. Higgins, S. A. Jaffer, T. F. Jaramillo, and E. H. Sargent, What would it take for renewably powered electrosynthesis to displace petrochemical processes?, *Science* **eaav364**, 3506 (2019).
 - [2] I. E. L. Stephens, *et al.*, 2022 roadmap on low temperature electrochemical CO_2 reduction, *J. Phys.: Energy* **4**, 042003 (2022).
 - [3] D. Wakerley, S. Lamaison, J. Wicks, A. Clemens, J. Feaster, D. Corral, S. A. Jaffer, A. Sarkar, M. Fontecave, E. B. Duoss, S. Baker, E. H. Sargent, T. F. Jaramillo, and C. Hahn, Gas diffusion electrodes, reactor designs and key metrics of low-temperature CO_2 electrolysers, *Nat. Energy* **7**, 130 (2022).
 - [4] S. Nitopi, E. Bertheussen, S. B. Scott, X. Liu, A. K. Engstfeld, S. Horch, B. Seger, I. E. L. Stephens, K. Chan, C. Hahn, J. K. Nørskov, T. F. Jaramillo, and I. Chorkendorff, Progress and perspectives of electrochemical CO_2 reduction on copper in aqueous electrolyte, *Chem. Rev.* **119**, 7610 (2019).
 - [5] T. Burdyny and W. A. Smith, CO_2 reduction on gas-diffusion electrodes and why catalytic performance must be assessed at commercially-relevant conditions, *Energy Environ. Sci.* **12**, 1442 (2019).
 - [6] M. Sassenburg, M. Kelly, S. Subramanian, W. A. Smith, and T. Burdyny, Zero-gap electrochemical CO_2 reduction cells: Challenges and operational strategies for prevention of salt precipitation, *ACS Energy Lett.* **8**, 321 (2023).
 - [7] J. A. Rabinowitz and M. W. Kanan, The future of low-temperature carbon dioxide electrolysis depends on solving one basic problem, *Nat. Commun.* **11**, 5231 (2020).
 - [8] S. Ringe, C. G. Morales-Guio, L. D. Chen, M. Fields, T. F. Jaramillo, C. Hahn, and K. Chan, Double layer charging driven carbon dioxide adsorption limits the rate of electrochemical carbon dioxide reduction on gold, *Nat. Commun.* **11**, 33 (2020).
 - [9] G. Marcandalli, M. C. O. Monteiro, A. Goyal, and M. T. M. Koper, Electrolyte effects on CO_2 electrochemical reduction to CO, *Acc. Chem. Res.* **55**, 1900 (2022). PMID: 35772054,
 - [10] E. L. Clark and A. T. Bell, Direct observation of the local reaction environment during the electrochemical reduction of CO_2 , *J. Am. Chem. Soc.* **140**, 7012 (2018). PMID: 29756446,
 - [11] Y. Y. Birdja, E. Pérez-Gallent, M. C. Figueiredo, A. J. Göttle, F. Calle-Vallejo, and M. T. M. Koper, Advances and challenges in understanding the electrocatalytic conversion of carbon dioxide to fuels, *Nat. Energy* **4**, 732 (2019).
 - [12] X. Liu, P. Schlexer, J. Xiao, Y. Ji, L. Wang, R. B. Sandberg, M. Tang, K. S. Brown, H. Peng, S. Ringe, C. Hahn, T. F. Jaramillo, J. K. Nørskov, and K. Chan, pH effects on the electrochemical reduction of $\text{CO}_{(2)}$ towards C_2 products on stepped copper, *Nat. Commun.* **10**, 32 (2019).

- [13] G. Kastlunger, L. Wang, N. Govindarajan, H. H. Heenen, S. Ringe, T. Jaramillo, C. Hahn, and K. Chan, Using pH dependence to understand mechanisms in electrochemical CO reduction, *ACS Catal.* **12**, 4344 (2022).
- [14] H.-J. Peng, M. T. Tang, J. Halldin Stenlid, X. Liu, and F. Abild-Pedersen, Trends in oxygenate/hydrocarbon selectivity for electrochemical CO₂ reduction to C₂ products, *Nat. Commun.* **13**, 1399 (2022).
- [15] G. Kastlunger, H. H. Heenen, and N. Govindarajan, Combining first-principles kinetics and experimental data to establish guidelines for product selectivity in electrochemical CO₂ reduction, *ACS Catal.* **13**, 5062 (2023).
- [16] A. Xu, N. Govindarajan, G. Kastlunger, S. Vijay, and K. Chan, Theories for electrolyte effects in CO₂ electroreduction, *Acc. Chem. Res.* **55**, 495 (2022). PMID: 35107967,
- [17] S. Ringe, Cation effects on electrocatalytic reduction processes at the example of the hydrogen evolution reaction, *Curr. Opin. Electrochem.* **39**, 101268 (2023).
- [18] J. C. Bui, E. W. Lees, L. M. Pant, I. V. Zenyuk, A. T. Bell, and A. Z. Weber, Continuum modeling of porous electrodes for electrochemical synthesis, *Chem. Rev.* **122**, 11022 (2022). PMID: 35507321,
- [19] T. Moore, X. Xia, S. E. Baker, E. B. Duoss, and V. A. Beck, Elucidating mass transport regimes in gas diffusion electrodes for CO₂ electroreduction, *ACS Energy Lett.* **6**, 3600 (2021).
- [20] D. Bohra, J. H. Chaudhry, T. Burdyny, E. A. Pidko, and W. A. Smith, Modeling the electrical double layer to understand the reaction environment in a CO₂ electrocatalytic system, *Energy Environ. Sci.* **12**, 3380 (2019).
- [21] L.-C. Weng, A. T. Bell, and A. Z. Weber, Modeling gas-diffusion electrodes for CO₂ reduction, *Phys. Chem. Chem. Phys.* **20**, 16973 (2018).
- [22] M. R. Singh, J. D. Goodpaster, A. Z. Weber, M. Head-Gordon, and A. T. Bell, Mechanistic insights into electrochemical reduction of CO₂ over Ag using density functional theory and transport models, *Proc. Natl. Acad. Sci. U.S.A.* **114**, E8812 (2017).
- [23] T. Y. Lin, S. E. Baker, E. B. Duoss, and V. A. Beck, Analysis of the reactive CO₂ surface flux in electrocatalytic aqueous flow reactors, *Ind. Eng. Chem. Res.* **60**, 11824 (2021).
- [24] H. Wang, A. Thiele, and L. Pilon, Simulations of cyclic voltammetry for electric double layers in asymmetric electrolytes: A generalized modified Poisson–Nernst–Planck model, *J. Phys. Chem. C* **117**, 18286 (2013).
- [25] C. T. Campbell, The degree of rate control: A powerful tool for catalysis research, *ACS Catal.* **7**, 2770 (2017).
- [26] See Supplemental Material at <http://link.aps.org/supplemental/10.1103/PRXEnergy.2.033010> including Refs. [50–52] for additional details.
- [27] N. Govindarajan, G. Kastlunger, H. H. Heenen, and K. Chan, Improving the intrinsic activity of electrocatalysts for sustainable energy conversion: Where are we and where can we go?, *Chem. Sci.* **13**, 14 (2022).
- [28] N. B. Watkins, Z. J. Schiffer, Y. Lai, C. B. Musgrave, H. A. Atwater, W. A. Goddard, T. Agapie, J. C. Peters, and J. M. Gregoire, Hydrodynamics change Tafel slopes in electrochemical CO₂ reduction on copper, *ACS Energy Lett.* **2185** (2023).
- [29] A. L ev eque, Les lois de la transmission de chaleur par convection, *Ann. Mines* **13**, 201 (1928).
- [30] v. L. Graetz, Ueber die w armeleitungsf ahigkeit von fl ussigkeiten, *Ann. Phys.* **254**, 79 (1882).
- [31] P. N. Shah and E. S. Shaqfeh, Heat/mass transport in shear flow over a heterogeneous surface with first-order surface-reactive domains, *J. Fluid Mech.* **782**, 260 (2015).
- [32] P. N. Shah, T. Y. Lin, and E. S. Shaqfeh, Heat/mass transport in shear flow over a reactive surface with inert defects, *J. Fluid Mech.* **811**, 372 (2017).
- [33] N. M. Juhasz and W. M. Deen, Effect of local Peclet number on mass transfer to a heterogeneous surface, *Ind. Eng. Chem. Res.* **30**, 556 (1991).
- [34] J. C. Bui, C. Kim, A. J. King, O. Romiluyi, A. Kusoglu, A. Z. Weber, and A. T. Bell, Engineering catalyst–electrolyte microenvironments to optimize the activity and selectivity for the electrochemical reduction of CO₂ on Cu and Ag, *Acc. Chem. Res.* **55**, 484 (2022).
- [35] X. Zhu, J. Huang, and M. Eikerling, Electrochemical CO₂ reduction at silver from a local perspective, *ACS Catal.* **11**, 14521 (2021).
- [36] X. Zhu, J. Huang, and M. Eikerling, pH effects in a model electrocatalytic reaction disentangled, *JACS Au* **3**, 1052 (2023).
- [37] T. Y. Lin, S. E. Baker, E. B. Duoss, and V. A. Beck, Topology optimization of 3D flow fields for flow batteries, *J. Electrochem. Soc.* **169**, 050540 (2022).
- [38] T. Roy, M. A. S. d. Troya, M. A. Worsley, and V. A. Beck, Topology optimization for the design of porous electrodes, *Struct. Multidiscip. Optim.* **65**, 171 (2022).
- [39] M. D. R. Batista, S. Chandrasekaran, B. D. Moran, M. S. d. Troya, A. Pinongcos, Z. Wang, R. Hensleigh, A. Carleton, M. Zeng, T. Roy, D. Lin, X. Xue, V. A. Beck, D. A. Tortorelli, M. Stadermann, R. Zheng, Y. Li, and M. A. Worsley, Design and additive manufacturing of optimized electrodes for energy storage applications, *Carbon* **205**, 262 (2023).
- [40] A. M. Limaye, J. S. Zeng, A. P. Willard, and K. Manthiram, Bayesian data analysis reveals no preference for cardinal Tafel slopes in CO₂ reduction electrocatalysis, *Nat. Commun.* **12**, 703 (2021).
- [41] J. Huang, X. Zhu, and M. Eikerling, The rate-determining term of electrocatalytic reactions with first-order kinetics, *Electrochim. Acta.* **393**, 139019 (2021).
- [42] A. J. Medford, C. Shi, M. J. Hoffmann, A. C. Lausche, S. R. Fitzgibbon, T. Bligaard, and J. K. N orskov, CatMAP: A software package for descriptor-based microkinetic mapping of catalytic trends, *Catal. Lett.* **145**, 794 (2015).
- [43] R. G. Mariano, K. McKelvey, H. S. White, and M. W. Kanan, Selective increase in CO₂ electroreduction activity at grain-boundary surface terminations, *Science* **358**, 1187 (2017).
- [44] K. Chan and M. Eikerling, A pore-scale model of oxygen reduction in ionomer-free catalyst layers of PEFCs, *J. Electrochem. Soc.* **158**, B18 (2010).
- [45] F. Rathgeber, D. A. Ham, L. Mitchell, M. Lange, F. Luporini, A. T. T. McRae, G.-T. Bercea, G. R. Markall, and P. H. J. Kelly, Firedrake: Automating the finite element method by composing abstractions, *ACM Trans. Math. Softw.* **43**, 24:1 (2016).

- [46] T. Roy, J. Andrej, V. Beck, V. Ehlinger, N. Govindarajan, and T. Lin, LLNL/echemfem: EchemFEM (2022).
- [47] T. Roy, J. Andrej, and V. A. Beck, A scalable DG solver for the electroneutral Nernst-Planck equations, *J. Comput. Phys.* **475**, 111859 (2023).
- [48] A. N. Brooks and T. J. Hughes, Streamline upwind/Petrov-Galerkin formulations for convection dominated flows with particular emphasis on the incompressible Navier-Stokes equations, *Comput. Methods Appl. Mech. Eng.* **32**, 199 (1982).
- [49] H. C. Elman, D. J. Silvester, and A. Wathen, *Finite Elements and Fast Iterative Solvers*, 2nd ed., Numerical Mathematics and Scientific Computation (Oxford University Press, London, England, 2014).
- [50] C. Geuzaine and J.-F. Remacle, Gmsh: A 3-D finite element mesh generator with built-in pre- and post-processing facilities, *Int. J. Numer. Methods Eng.* **79**, 1309 (2009).
- [51] G. Astarita, D. Savage, and A. Bisio, *Gas Treating with Chemical Solvents*, A Wiley-Interscience publication (John Wiley, 1983).
- [52] K. G. Schulz, U. Riebesell, B. Rost, S. Thoms, and R. Zeebe, Determination of the rate constants for the carbon dioxide to bicarbonate inter-conversion in pH-buffered seawater systems, *Mar. Chem.* **100**, 53 (2006).
- [53] <https://doi.org/10.5281/zenodo.8239837>
- [54] <https://doi.org/10.5281/zenodo.8263914>